Dynamic Sensitivities to Fractal Machine Noises in a Mechanical Face Seal

Itzhak Green
Fellow ASME
Woodruff School of Mechanical Engineering,
Georgia Institute of Technology,
Atlanta, GA 30332
e-mail: itzhak.green@me.gatech.edu

Mechanical face seals are wide spread in many applications of powered equipment and turbomachinery. Often machine vibration and noise are unavoidable because of changing conditions which can be persistent and forceful. In critical applications when seals fail, they may have significant or even catastrophic consequences. To ensure the safety of such machinery and its associated mechanical components, machine vibration and noise must be diagnosed and quantified to keep the system's response within certain limits. This work focuses on the dynamics of a flexibly mounted stator mechanical face seal that is subjected to combinations of broad-band noisy vibrations of the shaft and the housing. In all previous work, the positions of the housing and the shaft have been considered fixed. The current work relaxes that condition, augmenting the equations of motion to incorporate equipment's noisy vibrations. Noises are expediently produced by the Weierstrass–Mandelbrot (WM) fractal function. A numerical simulation ensues, and the time-domain responses are subject to spectral analyses. Results show that under some design conditions, the seal is largely insensitive to machine vibrations. However, under other conditions, the seal response to exterior machine noise exhibits a rich spectral content that stems from various transient phenomena that include intensified half-frequency whirl, near synchronous response at steady-state, and super-synchronous higher harmonic oscillations caused by face contact. [DOI: 10.1115/1.4056194]

Keywords: Weierstrass–Mandelbrot fractal function, mechanical face seals, dynamics, machine noise and vibration, frequency response, rubbing contact, machine dynamics, machinery and structural damage identification, machinery noise, mechanical signatures, nonlinear vibration, random vibration, rotor dynamics

1 Introduction

Mechanical face seals are wide spread in many applications, such as centrifugal compressors, submersible pumps, drill-bits for oil and water exploration, hydrocarbon processing machinery, pulp plants dryers, dry-gas seals in powered equipment and turbomachinery. Mechanical face seals are complex systems, where dynamics, fluid-film hydrodynamics, and thermoelastic effects are present and coupled to each other. A successful seal design must be tolerant for all these effects to co-exist. Over the last four decades, successful models have incorporated such effects singularly or collectively, including transient operations, but invariably they have all considered the surrounding to be pristine. Frequently, however, machines in which seals operate are subject to autonomous vibration. The seals inevitably respond to such vibration in manners that can be quite substantial and perhaps even destructive.

Very few previous works consider equipment noise and vibrations as they affect seals. Durham et al. [1] provide data from field installations of electric submersible pumps. They conclude that equipment vibration is inherent in seal design, manufacture, and application. A large percentage of pump failures may be attributed to seals that are unable to withstand high vibration, ultimately leading to motor and pump failures. Kim et al. [2] experimentally study the squeal noise and vibration of a mechanical seal used in an automotive water pump. The frequency spectra of both noise and vibration signals are obtained for various speeds of the pump, and waterfall plots for noise and vibration are constructed showing a relation between the natural frequencies, excitation frequencies, and squeal noise frequencies. Stefanko and Leishear [3] experimentally show that a reduction of radial vibrations in mechanical seals increases the life of the seals in centrifugal pumps. Many testimonies, gathered from end-users and seals' original equipment manufacturers, describe the dire consequences that machine vibration have upon seals' survivability. Most of these testimonies are hearsay of personal experiences; nevertheless, these effects do exist and must be understood.

The objective here is, therefore, to extend computational means to investigate the transient dynamic behavior of mechanical face seals subject to machine vibration. The analysis herein augments comprehensive models that have already been developed [4–37]. The said models included angular and axial modes of dynamic response in transient and steady-state operations [29,31,35,38], face transient warping, i.e., time-varying coning incorporated via transient thermoelastic deformation [39,40], and rough surface elasto-plastic contact of the seal faces [36]. All these effects had been coupled in a comprehensive model that simulates start-up to shut-down transient operation [41]. The theoretical models and numerical techniques [4–9,11–14,19,20,23,24,26–31,33–38,41] have been thoroughly verified through extensive experimentation [10,15,17,18,21,22,25,26,28,32,42]. These theoretical models provide the foundation for the current analysis. While in all of the previous analyses the seal enclosure is assumed to be inertial, here, that condition is relaxed. The current study expands the theoretical models, the computational means, and the diagnostics markers that are typical in the dynamics of flexibly mounted stator mechanical face seals, as they are affected by broad spectrum machine vibration (noise).

Machine noise can be simulated in various ways (or options): (1) by white noises using a random number generator, however, their time derivatives, which are categorically necessary in this work, are hard to come by (for reasons that are detailed in Ref. [43]),

Contributed by the Noise Control and Acoustics Division of ASME for publication in the Journal of Vibration and Acoustics. Manuscript received April 29, 2022; final manuscript received November 2, 2022; published online December 12, 2022. Assoc. Editor: Costin Untaroiu.

(2) by applying a collection of harmonics having random amplitudes, phases, and frequencies within respective frequency ranges of interest, in a process that resembles the method in Ref. [33], only that all harmonics are to be applied simultaneously to form time series of forcing harmonics, and (3) by a Weierstrass–Mandelbrot (WM) fractal function along with its time derivatives [44]. The availability of said derivatives (as discussed within) makes the WM fractal function particularly useful in the solution scheme. While the latter two options are successfully implemented in this work, option (3), which is a subclass of option (2), is considerably more convenient to implement numerically. That adaptation to noise generation is novel, and it is detailed herein. The said seal system serves as a dynamic testbed for executing this approach.

Because an analytical closed-form solution that accounts for all of the effects is patently not feasible, the investigation herein offers a comprehensive nonlinear numerical simulation for the transient response of a face seal that is subjected to its own forcing misalignments, and now as well, machine vibration (noise). The nonlinear nature of the problem is due to intermittent face (asperity) contact, cavitation, and large axial and angular excursions. The numerical procedure is outfitted with the most robust contact model by Jackson and Green [45,46]. Another novel approach is taken: for balanced mechanical seals, face roughness is largely unaltered by contact, whenever it ever happens. Correspondingly, a time-invariant curve-fit is introduced to relate the contact force to the film thickness by an explicit expression. That removes the need to re-deploy the contact model at each time-step during the simulation, which vastly reduces the computational effort. In the end, simulation results are provided to assess the sensitivities to noise of the most important seal performance outcomes, such as the axial seal face excursion, the relative tilt between the stator and the rotor, the minimum film thickness, and the leakage.

2 The Model for the Analysis

This work fully builds upon all of the aforementioned analyses, with Ref. [41] being the foundation, and hence, the modeling sections on face deformation caused by mechanical and thermal effects, the kinematics, and the method of solution remain intact (see details in Ref. [41]). However, significant expansions and enhancements are made. Some of the changes stem from the noises imparted by the rotor and housing mechanical vibrations.

Figure 1 shows the schematics of a mechanical seal. Parameters are described in the nomenclature and elaborated in Ref. [41]. The stator is the flexibly mounted (floating) face and it is supported by circumferentially distributed springs, while the rotor is a face fixed to the rotating shaft. A kinematical model is shown in Fig. 2, where detailed model descriptions are given in Refs. [5–7,29,35,41], and those remain intact. Briefly, the coordinate system *XYZ* is inertial, while the rotating system *xyz* is where the angular position of the stator is expressed using the Euler angles, the nutation γ_s, the precession, ψ, and the spin, ϕ. The spin is reduced via the kinematical constraint that is imposed by the secondary seal and locking devices [6,35]. The upcoming equations of motion (EOMs) use the said angles (as expressed in Sec. 2.5).

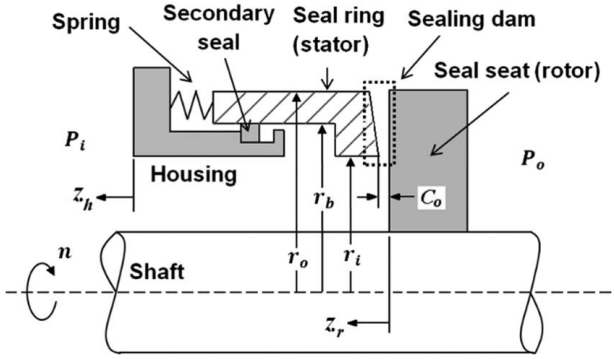

Fig. 1 Mechanical face seal schematics showing rotor and housing random excitations (noises) Z_h and Z_r, respectively

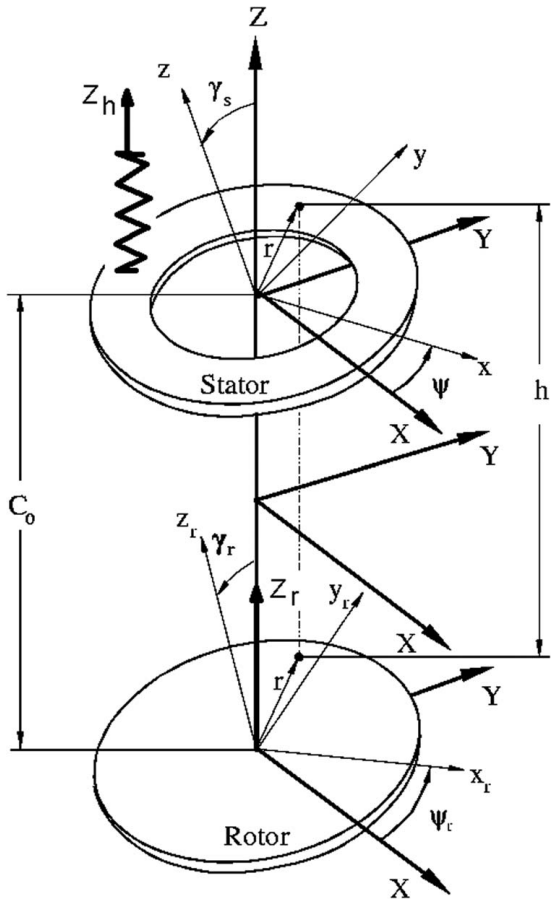

Fig. 2 A kinematical model showing excitations Z_h and Z_r

Of importance here is the stator responses, γ_{sI}, to its own initial misalignment and to the rotor runout, γ_{sr}. They are superimposed vectorially to yield the total stator misalignment:

$$\vec{\gamma}_s = \vec{\gamma}_{sI} + \vec{\gamma}_{sr} \tag{1}$$

The relative tilt between the seal faces is measured between the total stator response given by Eq. (1) and the rotor runout γ_r. As observed in a rotor-fixed coordinate system, that is:

$$\vec{\gamma} = \vec{\gamma}_s - \vec{\gamma}_r;\ |\gamma| = [\gamma_s^2 + \gamma_r^2 - 2\gamma_s\gamma_r\cos(\psi - \psi_r)]^{1/2},\ \ \psi_r(t) = \int_0^t \dot{\psi}_r dt \tag{2}$$

That relative tilt is needed for the calculation of the film thickness $h(r, \theta, t)$, shown in Fig. 2. As implied, the film thickness, in general, varies with the radial and circumferential coordinates, r and θ, respectively, and the time, t, via the responses of the degrees-of-freedom to forcing. The circumferential coordinate, θ, is measured from a reference axis defined by the relative tilt unit vector, $\hat{\gamma} = \vec{\gamma}/|\gamma|$. Mathematically, $h(r, \theta, t)$ is expressed in Sec. 2.4.

2.1 Asperity Contact and Thermoelastic Deformation. The seal clearance at the sealing dam is typically the order of a micron or even a submicron in modern applications. This is where asperity contact compounded with face deformation would have significant effects on performance. Seal leakage and wear (survivability) are

Table 1 Reference case

$r_i = 0.0355$ m	$r_o = r_g = 0.0408$ m	$\gamma_{si} = 0.5 \times 10^{-3}$ rad	$\gamma_r = 0.5 \times 10^{-3}$ rad
$K_{Zs} = 5 \times 10^5$ N/m	$D_{Zs} = 300$ N s/m	$F_{\text{spring}} = 20$ N	$m = 1$ kg
$\beta_{\text{ref}} = 5 \times 10^{-6}$ rad	$h_{\text{ref}} = 0.3 \times 10^{-6}$ m	$\omega_{\text{ref}} = 500$–$3000$ rad/s	$\beta(0) = 0$ rad
$\mu = 1.2 \times 10^{-3}$ Pa·s	$R = 1.7 \times 10^{-6}$ m	$S_y = 360$ MPa	$C_o = 10^{-6}$ m
$E = 24.07$ GPa	$\sigma = 10^{-7}$ m	$\psi = 6.167$	$\eta = 4.16 \times 10^{11}$ asp./m^2
$p_i = 100$ kPa	$p_o = 500$ kPa	$\tau = 2$ s	$B = 0.75$

two competing design objectives that are strongly influenced by asperity contact and face deformation.

For the lack of a better model at the time, the asperity contact model used in Ref. [41] is based upon Chang et al.'s elasto-plastic model [47], a model that is now obsolete [48]. The contact elasto-plastic model adopted herein is that by Jackson–Green [45] being the most robust and precise to date. The statistical accumulation of all asperity effects is done according to Ref. [46]. Now, an additional departure from the approach in Ref. [41] is offered. An off-line curve-fit is used for numerical expediency [36,49] expressing the local (nodal) contact pressure versus fluid-film thickness, $h(r, \theta, t)$. The rationale for the approach and the procedure are summarized in the Appendix. Hence,

$$p_c(r, \theta, t) = C_1 \exp\left[-C_2 h(r, \theta, t)\right] \tag{3}$$

where C_1 and C_2 are fit parameters specific to the seal faces roughness and their material properties as given in Table 1. The procedure outlined in the Appendix renders $C_1 = 3.5 \times 10^9$ Pa, and $C_2 = 2.8 \times 10^7$ m^{-1}. Hence, at any instant in time, and for any localized value of $h(r, \theta, t)$, the localized contact pressure, $p_c(r, \theta, t)$, is expediently calculated by Eq. (3). Notably, that equation offers a continuous, and a more realistic, transition from noncontacting to contacting operation and vice versa (instead of a commonly used on-off switch such as the Heaviside function).

Seal face coning, $\beta = \beta(t)$, is affected by the time-dependent thermoelastic deformations. The coning is schematically shown in Fig. 1 by the tapered sealing dam. Shaft rotation distributes the heat generation about the seal surfaces, allowing the thermoelastic deformations to be governed by a first-order ordinary differential equation [41]:

$$\tau\dot{\beta} + \beta = \beta_{\text{ref}}\left[\left(\frac{h_{\text{ref}}}{\bar{h}(t)}\right)\left(\frac{\omega_r(t)}{\omega_{\text{ref}}}\right)^2 + \frac{H_f}{(H_v)_{\text{ref}}}\right] \tag{4}$$

where τ is a thermal time constant (the smaller it is, the faster is the coning response), and H is the heat generation caused by friction and viscous effects. The reference coning, β_{ref}, and the time constant, τ, are obtained from an off-line transient finite element analysis of heat transfer of the entire seal assembly for a reference film thickness, h_{ref} (see Table 1). The average film thickness, $\bar{h}(t)$, and the shaft speed, $\omega_r(t)$, may be time-dependent, as they are in this work. The first term on the right-hand side of Eq. (4) is caused by the viscous heat generation, while the second term originates from traction, i.e., the result of a friction coefficient, f, and the contact pressure, p_c. Both heat generation mechanisms are

$$\begin{aligned} H_f &= \int_0^{2\pi}\int_{r_i}^{r_o} f p_c(r, \theta, t)\omega_r(t) r^2 dr d\theta \\ (H_v)_{\text{ref}} &= \int_0^{2\pi}\int_{r_i}^{r_o} \frac{\mu\omega_{\text{ref}}^2}{h_{\text{ref}}} r^3 dr d\theta \end{aligned} \tag{5}$$

Clearly, H_f is effective only if contact occurs, and that the contact pressure, p_c, is meaningful compared to the fluid pressure. Incompressible fluids commonly have a relatively high viscosity (see the viscosity of water at 20 °C in Table 1), so that the reference viscous heat generation, $(H_v)_{\text{ref}}$, is orders of magnitude larger than any friction-induced heat, H_f. Hence, the second term on the right-hand side of Eq. (4) may judicially be neglected. That is not so for gas-lubricated seals, where the viscosity of gas is relatively low (about two orders of magnitude lower than water), and H_f may become increasingly significant. Nevertheless, Eq. (5) represents the temporal accumulation of all local (nodal) heat generations, and those are calculated within the time integration scheme. Equation (4) will be placed in the upcoming state-space formulation to be time-integrated alongside with the equations of motion.

2.2 Noise Excitation. This section contains key kinematical changes viz-à-viz the model in Ref. [41], which are caused by rotor and housing random vibrations. These noises impose additional forcing mechanisms in the Reynolds equation, and the equations of motion, which are now being detailed.

Two forcing excitations are shown in Figs. 1 and 2. The machine (i.e., housing) may have an axial vibration, Z_h, along with an axial vibration of the shaft (i.e., rotor), Z_r, where both may occur synchronously or asynchronously. The former applies when the shaft is riding on bearings attached to the housing, which is the case considered here. A kinematical model is shown in Fig. 2, the fundamentals of which are given in Refs. [5,7,29,35,41], and those remain intact. While Z_r affects directly the film thickness, Z_h forces the stator axially via many springs that are circumferentially distributed. Only one of those springs is shown in Fig. 2, but effectively it represents all springs.

In addition to the said two axial noises, the shaft, due to its flexibility, might contain a noisy (time-varying) runout:

$$\vec{\gamma}_r = [\gamma_r + \delta_r(t)]\hat{\gamma}_r \tag{6}$$

where $\delta_r(t)$ represents the noisy part of the rotor runout. In the current model, however, the machine vibrations are assumed to take place mainly in the axial direction. Nonetheless, because of the physical coupling between the axial and the angular modes, *all modes* experience noisy operation (as the results will show). Hence, it is presumed that $\delta_r(t) = 0$.

2.3 Noise Signal Modeling. As discussed in Sec. 1, the noises, Z_h and Z_r, can be simulated in various ways. Here, the WM fractal function offers a systematic approach to simulate broad spectrum noises along with their analytic time derivatives [44]. As it is outlined below in Sec. 2.4, the time derivatives of the noise are categorically needed in the current analysis, and they must be exact outcomes of the noisy signal itself. The approach herein to noise generation is novel, and it is now detailed.

The WM fractal noises can be deterministic (default) or random (if random phases are added [50]). The noises herein for the housing (Z_h) and/or the rotor (Z_r) are generated deterministically following [44]

$$\left.\begin{aligned} Z_a(t) &= A_a \cdot \sum_{n=n_1}^{n_2} g^{(D-2)n}\cos\left(g^n t\right) \\ \dot{Z}_a(t) &= -A_a \cdot \sum_{n=n_1}^{n_2} g^{(D-1)n}\sin\left(g^n t\right) \end{aligned}\right\} \quad 1 < D < 2; \quad g > 1; \qquad a = h \text{ or } r \tag{7}$$

where g^n sets off a geometrically increasing series of frequencies. The noise scale is A_a, taken here as 1% of the designed seal clearance, C_o (where A_a can either be different for Z_h and Z_r, or the same,

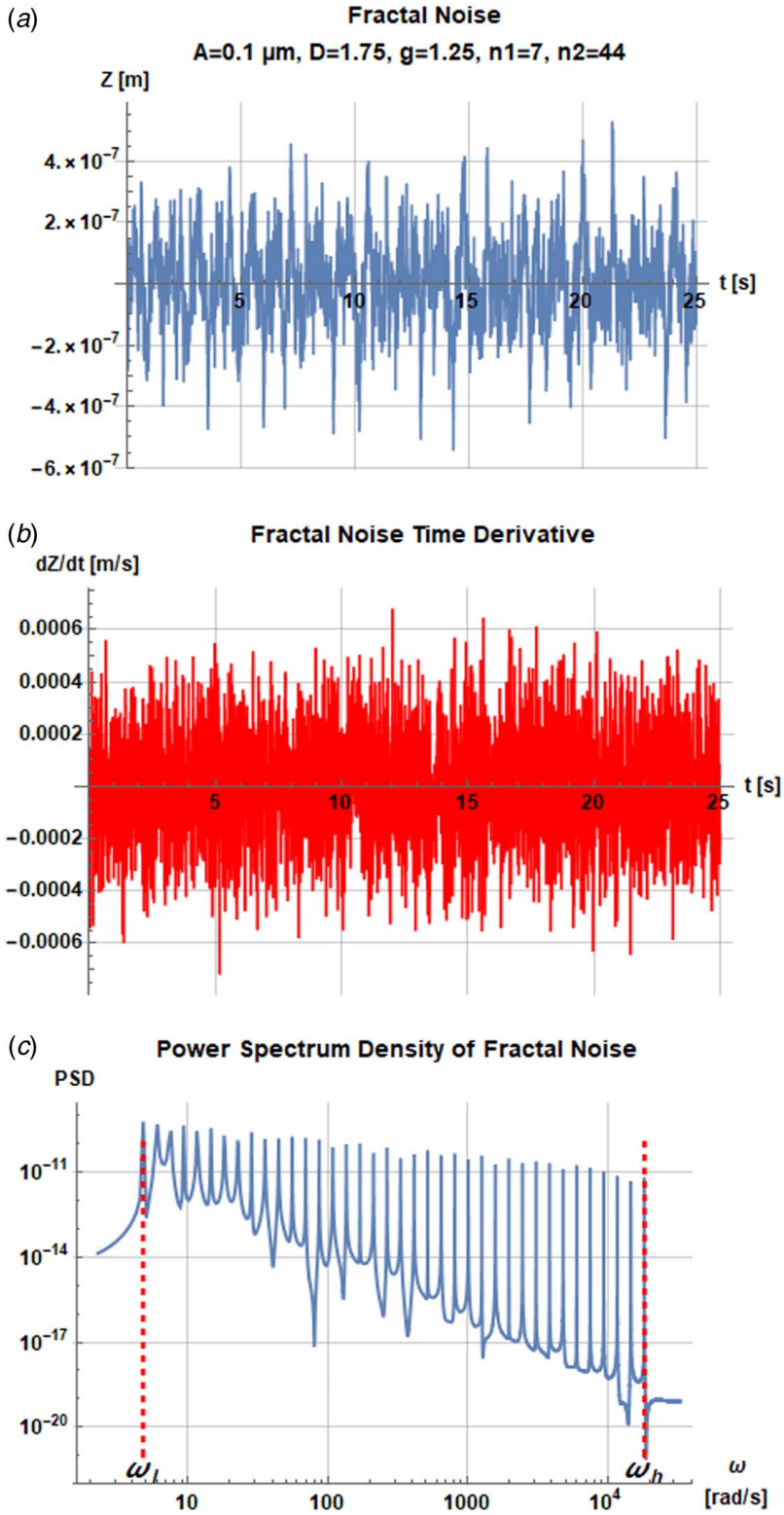

Fig. 3 Noise versus time (*a*), its time derivative (*b*), and PSD (*c*)

i.e., $A_a \equiv A$ as implemented herein). The frequency range of interest is earmarked between a low value (ω_l) and a high value (ω_h). Via $\omega \leftrightarrow g^n$, these frequencies determine the summation limits n_1 and n_2 in Eq. (7):

$$n_1 = \text{Floor}[\ln(\omega_l)/\ln(g)]$$
$$n_2 = \text{Floor}[\ln(\omega_h)/\ln(g)] + 1 \tag{8}$$

where Floor[x] gives the greatest integer less than or equal to x; so, n_1 is rounded down, while n_2 is rounded up. For the frequency range of interest (see Table 1), the low and high frequencies are, respectively, set as $\omega_l = 0.01 \times 500 = 5$ rad/s and $\omega_h = 5 \times 3000 = 15{,}000$ rad/s. Using also $D = 1.75$ and $g = 1.25$, these result in $n_1 = 7$ and $n_2 = 44$.

There is a widespread notion about the WM function that presumes it to be "non-differential" (e.g., see Ref. [50]). Green [44]

mathematically shows that that is indeed so *only* when the summation bounds in the WM function are let to approach infinity. That, however, is practically (i.e., numerically) impossible to implement nor is it physically necessary. As employed above, the bounds n_1 and n_2 are finite. Under these conditions, derivatives of the WM function *do exist*. That is an important point that must be appreciated because only temporal time derivatives are needed here, regardless of whether the sums of the derivatives of the WM function converge. Stressing this point further, while series convergence of Eq. (7), is principally important in Ref. [44] (because the integrals of which are the actual final objectives there), that is inconsequential here because the need is just for temporal values. The summation of Eq. (7) may thus be interpreted as being a "collection" or an "ensemble" that produces temporal values without regards or need for it to be further integrated (as is the case in Ref. [44]). In summary, the issue of the WM function differentiability is moot in this work. Hence, the WM function itself and its derivatives do produce temporal values for any finite n_1 and n_2, and their convergence is of no significance.

Figure 3(*a*) shows a fractal noise, along with its time derivative in Fig. 3(*b*), using the said fractal parameters in an arbitrary time span, 0–25 s. For the time derivative, the noise scale A is progressively amplified within the series (summation) by g^n, so its root mean square (RMS $= 2\times10^{-4}$ m/s) is more than three orders of magnitude larger than that of the noise itself (RMS $= 1.5\times10^{-7}$ m). The latter is designated as z_a, being the RMS value of the noise, and it will be used to normalize transmissibilities which also serve as sensitivities. The higher magnitudes of the noise derivatives may well impress upon the ensuing dynamics via the fluid-film and support damping properties.

Clearly, any desired noise characteristics can be generated by simply altering the fractal parameters in Eq. (7). A smaller g produces a denser spectrum as it also determines the progressive amplitude change between the spectral modes, while a larger fractal dimension D produces a more jagged noise. While the WM fractal function given by Eq. (7) is deterministic, a plausible way to produce randomness in the noises' amplitudes is to add random phases as discussed in Ref. [50], however, the spectral content remains unaltered. There are five parameters that construct the WM function in Eq. (7) such that a great number of noise patterns can be generated by altering any one, or any number of those. In the forgoing, Z_h and Z_r along with their time derivatives are deemed available by way of Eqs. (7) and (8) and is shown in Fig. 3 (the power spectral density (PSD), shown in Fig. 3(*c*), will be discussed in Sec. 2.6).

It is also recognized that if the noise scale, A, is set identically to zero ($A=0$), the functions in Eq. (7) are nullified. Operation in the absence of any noise is referred to as a "pristine operation," and that is put to use in Sec. 2.5.

2.4 The Effects of Housing and Rotor Vibration. The film thickness, h, shown in Fig. 2, is a function of position and time [5,7,29,41], where now it is modified to include the rotor axial noise, $Z_r(t)$:

$$h(r,\theta,t) = C_o + [Z(t) - Z_r(t)] + \gamma(t) r\cos(\theta) + \beta(t)(r - r_i) \tag{9}$$

The spatial and time derivatives, with the latter including the shaft axial noise derivative, $\dot{Z}_r(t)$, are

$$\frac{\partial h(r,\theta,t)}{\partial\theta} = -\gamma(t) r\sin(\theta)$$
$$\frac{\partial h(r,\theta,t)}{\partial t} \equiv \dot{h}(r,\theta,t) = [\dot{Z}(t) - \dot{Z}_r(t)] + \dot{\gamma}(t) r\cos(\theta) + \dot{\beta}(t)(r - r_i) \tag{10}$$

Note that $\dot{\beta}(t)$ is taken from Eq. (4). The film thickness is needed for the solution of the Reynolds equation for incompressible fluids [7,41]:

$$\vec{\nabla}\cdot\left[\frac{h^3\vec{\nabla}p_f}{12\mu} - \frac{1}{2}\omega r h\vec{i}_\theta\right] = \frac{\partial h}{\partial t} \tag{11}$$

The unknown is the fluid-film pressure, $p_f = p_f(r,\theta,t)$, reigning in the sealing dam (see Fig. 1). This equation is subject to initial and boundary conditions, where the latter can also be time-dependent (see details in Ref. [41]). Clearly, the fluid-film pressure, $p_f(r,\theta,t)$, depends upon $h(r,\theta,t)$, and thus upon the noise, $Z_r(t)$, by way of Eq. (9), while $\partial h(r,\theta,t)/\partial t$ depends also upon the noise time derivative, $\dot{Z}_r(t)$, by way of Eq. (10). Likewise, by way of Eqs. (9) and (10), the solution depends on the instantaneous values of $\gamma(t)$, $\beta(t)$, $\dot{\gamma}(t)$, and $\dot{\beta}(t)$ that are governed by Eqs. (1), (2), and (4). The solution of Eq. (11) for $p = p_f(r,\theta,t)$ is presented in closed-form by Green and Etsion [5,7]:

$$\begin{aligned} p_s(r,\theta,t) &= p_i - (p_i - p_o)\frac{h_o^2}{h_i^2 - h_o^2}\left[\left(\frac{h_i}{h}\right)^2 - 1\right] \\ p_d(r,\theta,t) &= -6\mu\left(\omega_r\frac{\partial h}{\partial\theta} + 2\frac{\partial h}{\partial t}\right)\frac{(r_o - r)(r - r_i)}{(h_i + h_o)h^2} \\ p_f(r,\theta,t) &= p_s(r,\theta,t) + p_d(r,\theta,t) \end{aligned} \tag{12}$$

where $\omega_r = \omega_r(t)$ is the time-dependent shaft speed. Cavitation, which adds to the nonlinearity of the problem, is handled by the half-Sommerfeld boundary condition. Pressures from potential asperity contact, p_c, are available from Eq. (3). The sealing dam is meshed to have 11 nodes in the radial direction and 37 nodes in the circumferential direction. Both pressures, $p_f(r,\theta,t)$ and $p_c(r,\theta,t)$, are added together at every node and integrated by numerical quadrature over the sealing dam area to yield film tilting moments and axial force:

$$\begin{aligned} M_{fx} &= \int_0^{2\pi}\int_{r_i}^{r_o}[p_f(r,\theta,t) + p_c(r,\theta,t)]\, r^2\sin\theta\, dr\, d\theta \\ M_{fy} &= -\int_0^{2\pi}\int_{r_i}^{r_o}[p_f(r,\theta,t) + p_c(r,\theta,t)]\, r^2\cos\theta\, dr\, d\theta \\ F_{fz} &= \int_0^{2\pi}\int_{r_i}^{r_o}[p_f(r,\theta,t) + p_c(r,\theta,t)]\, r\, dr\, d\theta \end{aligned} \tag{13}$$

Additional applied moments and force that act upon the flexibly mounted stator are given by Eq. (21) in Ref. [41]. These are now augmented to include the housing noise and its derivative, $Z_h(t)$ and $\dot{Z}_h(t)$:

$$\begin{aligned} M_{sx} &= -K_s(\gamma_s - \gamma_{si}\cos\psi) - D_s\dot{\gamma}_s \\ M_{sy} &= -K_s\gamma_{si}\sin\psi - D_s\dot{\psi}\gamma_s \\ F_{sZ} &= -K_{Zs}(Z - Z_h) - D_{Zs}(\dot{Z} - \dot{Z}_h) \end{aligned} \tag{14}$$

Note that K_s and D_s are the support angular stiffness and damping coefficients, while K_{Zs} and D_{Zs} are their corresponding axial counterparts. These are either obtained from experimentation [10,42] or estimated by finite element analyses (FEA) [12,13]. This is where the housing noise and its derivative, $Z_h(t)$ and $\dot{Z}_h(t)$, add forcing to the systems' dynamics.

2.5 Numerical Integration in Time of the Equations of Motion. The EOM and the time-dependent coning (of Eq. (4))

are cast in a state-space form, as given by Eq. (26) in Ref. [41]:

$$\frac{\partial}{\partial t}\begin{Bmatrix}\dot{Z}\\ Z\\ \dot{\gamma}_s\\ \gamma_s\\ \dot{\psi}\\ \psi\\ \beta\end{Bmatrix}=\begin{Bmatrix}(F_{sZ}+F_{fZ}-F_{cls})/m\\ \dot{Z}\\ (M_{sx}+M_{fx})/I+\dot{\psi}^2\gamma_s\\ \dot{\gamma}_s\\ [(M_{sy}+M_{fy})/I-2\dot{\psi}\dot{\gamma}_s]/\gamma_s\\ \dot{\psi}\\ \{\beta_{\text{ref}}[(h_{\text{ref}}/h)(\dot{\psi}_r/\omega_{\text{ref}})^2]-\beta\}/\tau\end{Bmatrix} \tag{15}$$

F_{cls} is the net closing force resulting from the circumferential springs, the balance radius, r_b, by way of the hydraulic balance ratio, B (as given in Table 1), and the inner and outer pressures as shown in Fig. 1 (see more details in Ref. [41]). The initial conditions are

$$\begin{aligned}&Z(0)=-0.65C_o,\quad \gamma_s(0)=\gamma_r\\ &\dot{Z}(0)=\dot{\gamma}_s(0)=\psi(0)=\dot{\psi}(0)=\beta(0)=0\end{aligned} \tag{16}$$

The EOMs are integrated in time simultaneously by an efficient multistep ordinary differential equation solver [51]. The EOM in Eq. (15) is expressed in a rotating frame xyz using the Euler angles of nutation, γ_s, precession, ψ, and spin, ϕ, which, as indicated, is reduced by the kinematical constraint imposed by the anti-rotation pins [6,35]. That frame choice follows more closely the whirl of the stator, and thus the numerical time integration is considerably more CPU expedient and efficient. The sealed pressure and shaft speed are ramped-up to simulate machine start-up to steady-state (or reference values) as detailed in Ref. [41]. The same sample seal is chosen here as well with parameters given in Table 1. However, two changes are made: (1) a span of shaft speed cases, ranging within 500–3000 rad/s in increments of 250 rad/s, is each simulated, and (2) each simulation is allowed to complete at least 10^4 cycles to gather sufficient datasets needed for a robust spectral analysis.

The EOMs cast here have a rather small-sized state-space set expressed in Eq. (15). That is because for an incompressible film, the Reynolds equation has a closed-from solution for the fluid-film pressure as given by (12). When a seal is purposed to operate in a compressible medium (e.g., dry-gas), a different form of the Reynolds equation needs to simultaneously be solved numerically alongside with the EOM because closed-form solutions are not available for the pressure field, which is also time-dependent and hereditary. The unknown time-dependent nodal pressures add enormously to the size of state-space set, and thus to the computational effort, as done in Refs. [29–31,33,34]. The noise generation, however, and all the forthcoming principles and tools associated with the sensitivity to noise quantification remain intact and applicable.

The numerical simulation produces time series data for the degrees-of-freedom, Z, γ_s, and ψ, and for the minimum film thickness, $h_{\min}$, as well as other important parameters, e.g., flow (leakage), Q, and coning, β. Because this work is interested in the net transient responses caused by machine noises about steady-state operation, each case is simulated twice: (1) once without any noise, $Z_h=Z_r=0$, (i.e., by setting $A=0$ in Eq. (7)) and hence, the results (the time signals) which are evidently identical to those in Ref. [41] are referred to as "pristine signals," and (2) with noises generated by Eq. (7), i.e., $Z_h\neq 0$, $Z_r\neq 0$, the results (the time signals) of which are called "total noisy signals." The targets herein are the differences between the two solutions, i.e., the "net noisy signals," which are obtained by

$$\begin{aligned}\Delta(t)\triangleq{}&\text{Net noisy signal}(t)=\text{Total noisy signal}(t)\\ &-\text{Pristine signal}(t)\end{aligned} \tag{17}$$

That approach is needed because responses to initial conditions alone do not provide equivalent solutions about steady-state for the reason that the system is highly nonlinear. More so, the pristine signal may contain frequencies that are intrinsic responses of the system, where indeed in the seal investigated herein (with data in Table 1), and because of the forcing misalignments, γ_{si} and γ_r, the pristine signal is oscillatory as it will be seen later. To truly obtain the net sensitivity to noise, those intrinsic responses have to be removed to eliminate bias. So, in the foregoing, the analysis pertains to the net signal as given by Eq. (17) for all degrees-of-freedom and the parameters of interest.

2.6 Spectral Analysis and Sensitivity to Noise. The spectral analysis adheres to the procedure outlined in Appendix B in Ref. [42]. The following is a brief summary of that procedure. Suppose that the output signal, $x=x(t)$, is the time response to an input noisy excitation, $y=y(t)$. Next, $X=X(\omega)$ and $Y(\omega)$ are calculated by (fast) Fourier transforms for both signals.

While for the fractal noise of Eq. (7), there is a closed-form expression for the power spectrum density (see Ref. [44]), a numerical PSD is nevertheless used for all signals to maintain an unbiased numerical uniformity. That PSD is shown in Fig. 3(*c*) for the said fractal noise. The fractal density, g, being the geometric common ratio, is clearly seen to separate the peaked frequencies (see the $n_2-n_1+1=38$ peaks in Fig. 3(*c*) located equidistantly on a logarithmic scale). Also visibly, the PSD largely fades outside the range of ω_l and ω_h, as it should. Complementing to the issue of differentiability, it is obvious that adding a term to the WM fractal function, where the new $n_2\to n_2+1$, just adds another frequency, expanding the frequency range by making ω_h larger. A similar role can be conferred upon n_1 to affect ω_l.

The signals, which are sampled according to the Nyquist folding frequency, are analyzed in blocks of time such that there are at least $m=100$ blocks, where $X(\omega)$ and $Y(\omega)$ are being averaged over all blocks. That reduces the statistical error by a factor of at least $m^{1/2}=10$. Welch's method of overlapping windowing is executed to yet double the number of averages. After averaging, the power spectral densities are

$$p_x(\omega)=\frac{2\delta_h}{N}|X(\omega)|^2;\quad p_y(\omega)=\frac{2\delta_h}{N}|Y(\omega)|^2 \tag{18}$$

where $N=2^{nfft}$ is the number points in each block, *nfft* is an integer (having a value of 10 or higher), and δ_h is the time interval between sampled points. The cross spectral density function is

$$p_{yx}(\omega)=\frac{2\delta_h}{N}Y^*(\omega)\cdot X(\omega) \tag{19}$$

where $Y^*(\omega)$ is the conjugate of $Y(\omega)$. All power spectra are additionally processed by the novel G-Exp filter in Ref. [43] to moderate spectral clatter. The transmissibility is defined as the ratio of output/input:

$$\alpha(\omega)=\frac{|p_{yx}(\omega)|}{p_y(\omega)} \tag{20}$$

The coherence function is also calculated based on p_x, p_y, and p_{yx} (see Ref. [42]), and it is verified to be close to unity (1) to ensure causality between output and input. Of interest here are the transmissibilities of the various parameters as calculated by Eq. (20), and these are reported below.

To add a perspective, the transmissibility expressed by Eq. (20) represents also the sensitivity of any given parameter to noise. That is because the input signal is always the noise, i.e., $y(t)\equiv$ noise (as applied by Eq. (7)) having an RMS, z_a, where the output signals are (one at a time) the parameters under investigation, i.e., $x(t)\equiv\Delta(t)$ (as calculated by Eq. (17)). Because both are differentially small, the transmissibility expressed by Eq. (20) is, in kind, a first derivative representation of the output with respect to the input. A detailed sensitivity analysis is performed by Dayan et al. [27] on a mechanical seal where indeed the sensitivity is mathematically expressed as a first derivative of an output parameter with respect to a variation in input. Therefore, the transmissibilities

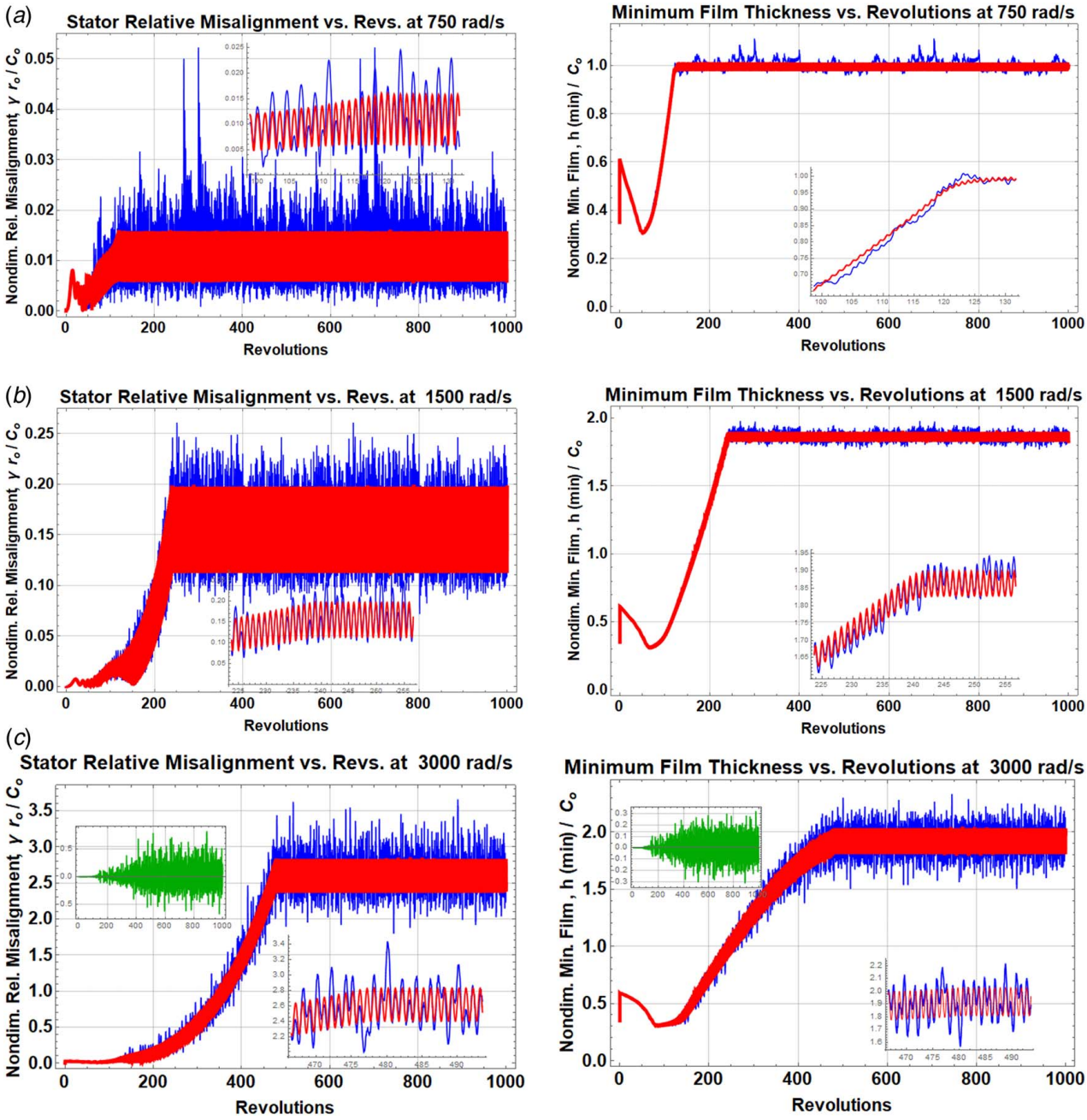

Fig. 4 Transients of nondimensional output parameters versus nondimensional time (revolutions) at three shaft speeds ω_{ref} = 750 (*a*), 1500 (*b*), and 3000 rad/s (c). Noisy transients are shown about the pristine signals with zommed-in ranges in insets. The net noisy signals are shown in the top-left insets for the highest shaft speed.

that will be discussed and analyzed below may also represent the sensitivities of the parameters to noise.

3 Results and Discussion

All results below are given in a nondimensional form. The time-domain transient results are shown in Fig. 4 for three specific shaft speeds, with corresponding frequency-domain transmissibilities shown in Fig. 5. Waterfall plots are shown in Fig. 6 for 3D representations of the net transmissibilities with respect to the shaft speed. The important parameters of coning (face warping) and leakage are lastly shown in Fig. 6 as well. Figure 7 shows waterfall plots for the same parameters as those in Fig. 6, only that the pristine responses have not been removed; hence, the plots in Fig. 7 represent the total transmissibilities.

Figure 4 shows the nondimensional transient responses versus normalized time (i.e., revolutions) for three shaft speed cases of $\omega_{ref} = 750$ (top), 1500 (middle), and 3000 rad/s (bottom). While information is available for all degrees-of-freedom, coning, flow, etc., only the most significant nondimensional parameters are shown. These are the relative tilts between stator and rotor, $\gamma r_o/C_o$, and the minimum film thicknesses, h_{min}/C_o. These two parameters are of prime importance in mechanical face seal operation as they determine the flowrates (leakages) and the likelihood of face contact—the larger these are, the larger the leakages and the likelihood of faces wear. In Fig. 4, the total noisy responses are shown to be larger than and surrounding, the pristine responses. Whereas in all analyses, at least 10^4 cycles have been simulated, but the plots show the (nondimensional) time signals only in a reduced range of up to 10^3 cycles. Past the start-up and initial transients, the periodic nature of all responses to noises forcing is also

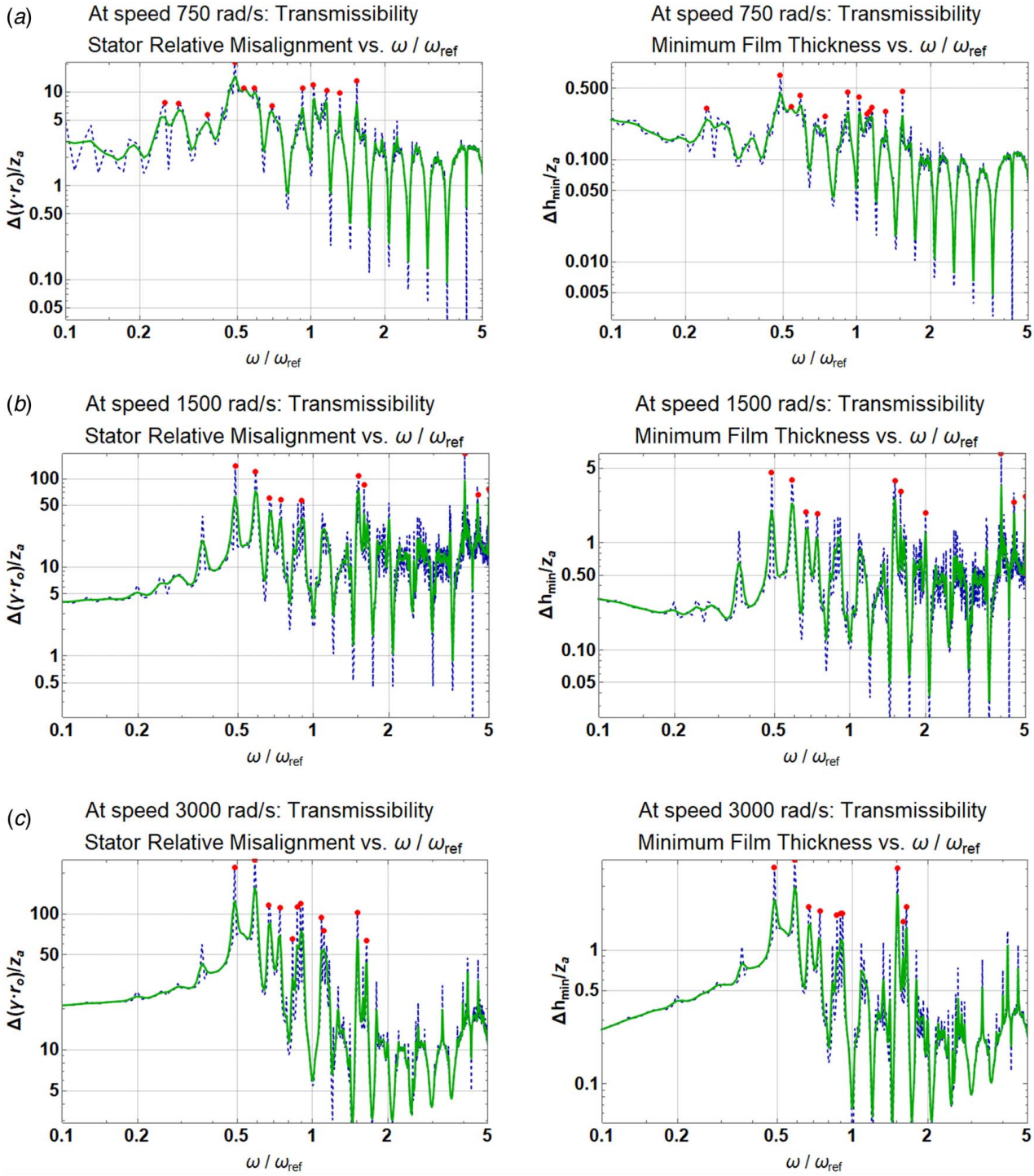

Fig. 5 Transmissibilities of cases in Fig. 4 versus frequency ratio, ω/ω_{ref}, at three shaft speeds $\omega_{ref} = 750$ (*a*), 1500 (*b*), and 3000 rad/s (c). Unfiltered signals are shown in dashed lines, and G-Exp filtered signals are shown in solid lines.

apparent, indicating that the signals settle to stable steady-state stationary forms. The signals past 10^3 cycles are gathered to provide sufficient data for robust signal processing (yet not shown).

In each case in Fig. 4, an inset is also shown at the transition from ramp-up to steady-state operation. Those insets show the oscillatory nature of the pristine signals (as discussed in Sec. 2.6). The wide bands are nothing other than the same pristine signals crammed together when shown on a larger scale. Turning to the physics, it is obvious that at the lower speed of 750 rad/s, the nondimensional relative misalignment, $\gamma \cdot r_o/C_o$, is very small, and the minimum film thickness, h_{min}, approaches the designed clearance, C_o. That is nearly an ideal state of operation. At that lower speed, the hydrodynamic effect and the inertial forces and moments are relatively small. Still the noisy response is quite apparent in the relative misalignment, which will also be evident in the transmissibilities shown in Fig. 5.

Still in Fig. 4, it is apparent that with the increase of the shaft speed, the nondimensional relative misalignments, $\gamma r_o/C_o$, and the nondimensional minimum film thickness, h_{min}/C_o, increase too. That is anticipated as the hydrodynamic and inertial effects increase with shaft speed. While the speed only doubled with each case in Fig. 4, the relative misalignments responses are

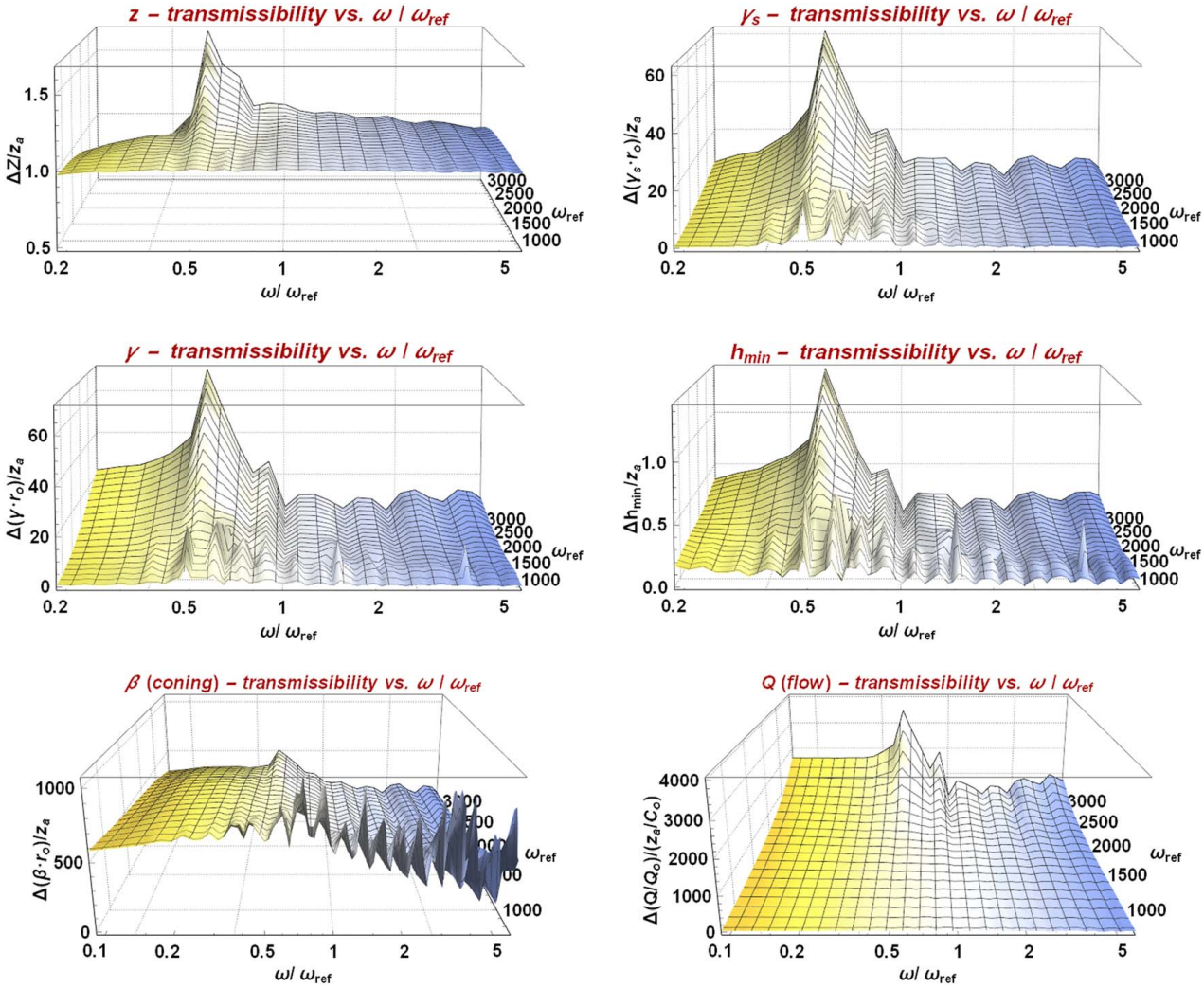

Fig. 6 Waterfall plots of parameters of *net* transmissibilities for the full range of shaft speeds, $\omega_{ref} = 500$–3000 rad/s

visibly much more than doubled (as envisaged from a nonlinear system). Also the minimum film thickness has increased, having a large increase from 750 to 1500 rad/s, and then a more moderate increase at 3000 rad/s. The relative tilt sees a much more dramatic increase with shaft speed. Clearly, at higher shaft speeds, the seal faces open up, having larger relative tilts, leading to increased leakages and perhaps even face contact (as discussed below).

For the highest shaft speed of 3000 rad/s, the net signals as obtained by Eq. (17) are also shown in other insets (at top-left corners). Similar behaviors are witnessed at other speeds. While limited statistical information can be extracted in the time-domain, e.g., the mean is verified to be zero obviously, the RMS (or the standard deviation) can be contrasted against the noise RMS; the spectral content, however, has to be obtained through a spectral analysis as outlined in Sec. 2.6. That is presented in Fig. 5, which shows on log–log scales the transmissibilities (i.e., the sensitivities) for the said parameters using Eq. (20). Some prominent peaks are also emphasized by the dots on top.

A quantity ("term") that is commonly used in rotordynamics is $nX = n(\omega/\omega_{ref})$, where n is an integer multiplier of the frequency ratio between the response and the shaft rotational speed. In all plots, the unfiltered noisy signal is shown in dashed lines, while filtered signals processed by the G-Exp filter as developed in Ref. [43] are shown by solid lines using filter parameters of $\beta_{G\text{-}Exp} = 4$ and $L = 3$. While the venerable Savitzy-Golay smoothing filter [52] has also been tried, it is the G-Exp filter that consistently produces superior results (similar to the outcomes in Ref. [43]) because the G-Exp can perpetually be tuned, while the Savitzky-Golay filter family is based on fixed-coefficients polynomials.

It is obvious that for all cases, the transients are consistently strong at sub-synchronous frequencies producing rich spectra, with the strongest responses occurring near the half-frequency whirl (or $\omega/\omega_{ref} = 1/2$, aka $X/2$), which is expected from the hydrodynamic effect [5,8,29,42]. Noticeable are also elevated responses about the synchronous speed, $\omega/\omega_{ref} = 1$ (i.e., at $1X$, which is also expected) especially at the higher speed of 3000 rad/s. At precisely $1X$, for all shaft speeds, the sensitivity to noise is reduced because the steady-state pristine response at that frequency is dominant anyway, where added noise does not produce relatively a meaningful contribution. Interestingly, even as the noises are generated only in the axial directions, because of the effective coupling between the axial and angular modes, the latter have much more powerful transmissibilities. The magnitudes of all transmissibilities increase with shaft speed, and quite considerably in the angular mode (i.e., in the nondimensional relative misalignments, $\gamma r_o/C_o$).

While the effects of the half-frequency whirl ($X/2$) is clearly evident by the strong peaks present at $\omega/\omega_{ref} = 1/2$, peaks are also prevalent at $\omega/\omega_{ref} = n/2$ (n being an integer multiplier). Peaks are also visible at super-synchronous frequencies being particularly prevalent at $1.5X$, $2X$, etc., and even more so at a higher shaft speed of 3000 rad/s. That behavior is a known attribute of seal faces rubbing in contact [15,36] as triggered by the noises.

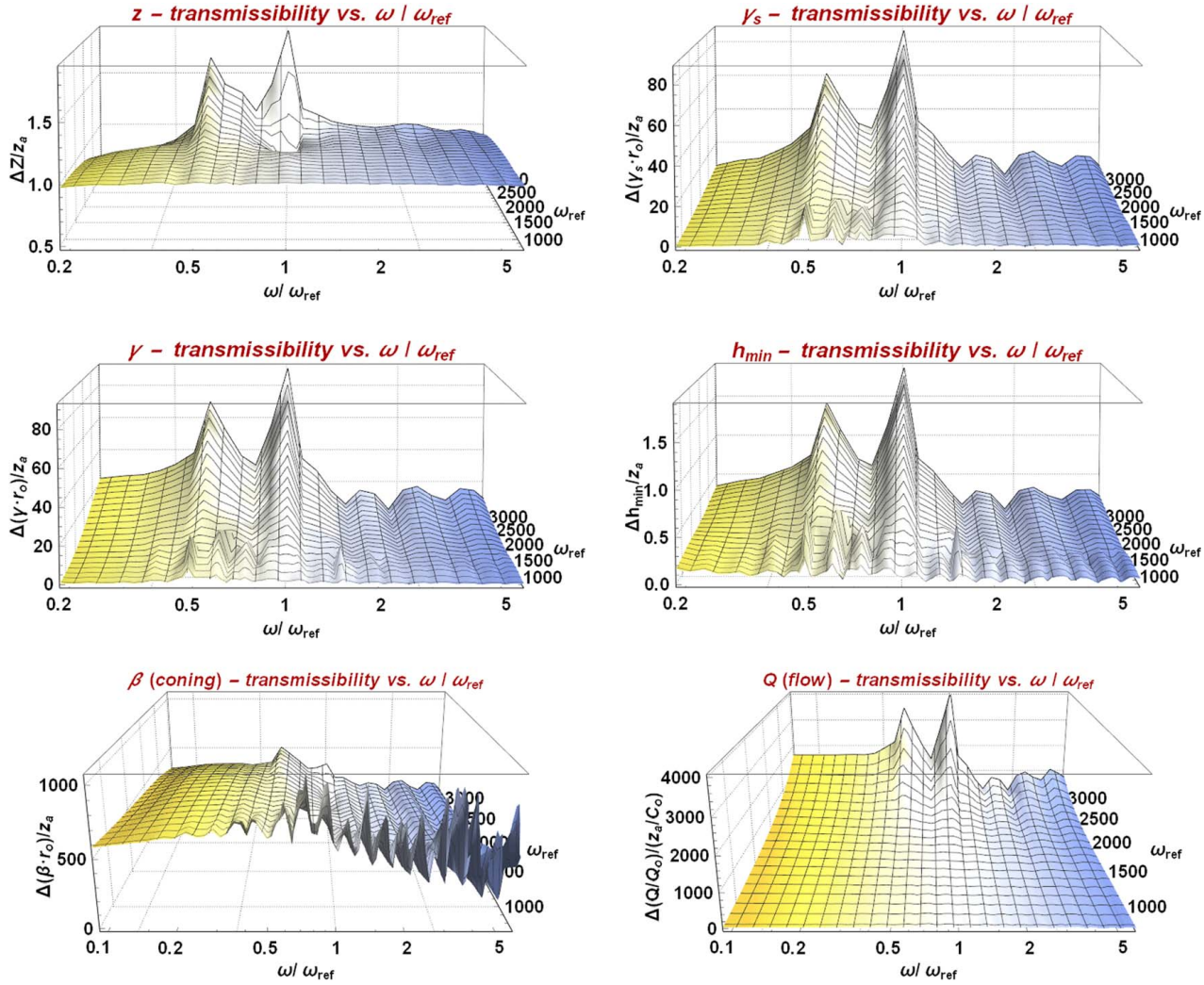

Fig. 7 Waterfall plots of the *absolute* transmissibilities for the full range of shaft speeds, $\omega_{ref} = 500$–3000 rad/s

The process that produces Figs. 4 and 5 is repeated for other shaft speeds, ω_{ref}, ranging from 500 to 3000 rad/s in increments of 250 rad/s. Figure 6 shows 3*D* waterfall plots of the normalized transmissibilities as calculated by Eq. (20) for the said parameters in that shaft speed range. That figure shows as an output of the transmissibility sensitivities to noise at various normalized response frequencies, ω/ω_{ref}. In addition to transmissibilities of the nondimensional relative misalignments, $\Delta\gamma r_o/C_o$, and the nondimensional minimum film thickness, $\Delta h_{min}/C_o$, also the transmissibilities for the axial degree-of-freedom, $\Delta Z/z_a$, and the nutation angle, $\Delta\gamma_s r_o/z_a$, are provided (where Δ corresponds to the net value obtained by Eq. (17)). There are meaningful transmissibility peaks at sub- and super-synchronous speeds. The strongest sensitivity is at and about the half-frequency whirl ($X/2$) or ($\omega/\omega_{ref} = 1/2$). Peaks at super-synchronous frequencies develop and prevail at shaft speeds of 2000 rad/s and become larger with the increase of shaft speeds.

The discoveries above underpin the outcomes for coning and flow transmissibilities also shown in Fig. 6. First, it is evident that coning sensitivities are increased at lower shaft speeds where the dynamic sensitivities (i.e., the responses of the other parameters) are relatively small. Large heat generation occurs at the smaller film thicknesses and vice versa. At the largest dynamic responses that cause larger film thicknesses, the flow, Q, is likewise large (see Fig. 6, paying attention to the scale). Large flows cool the seal surfaces and reduce the heat generation. Both compounded reduce coning sensitivities at the larger shaft speeds. The flow itself is normalized by the radial flow, Q_o, under ideal (and pristine) conditions having a designed and uniform film thickness, C_o, throughout. Hence, $Q_o = \pi C_o^3 (r_o + r_i)(p_o - p_i)/[12\mu(r_o - r_i)]$. The actual temporal flow, $Q(t)$, is proportional to the temporal film thickness to the third power $(Co + Z)^3$, to the relative tilt to the second power, γ^2, and to the coning, β. The flow is, therefore, magnified more intensely with the increase of all those three parameters, Z, γ, and β (as they are evident in Fig. 6). It is also apparent that the largest flow (leakage) sensitivities to noise occur correspondingly at $X/2$ (i.e., at half-frequency whirl) and predominantly again at shaft rotational speeds above 2000 rad/s.

The role of the "pristine" operation is understood from analyzing Fig. 7. That figure shows the results of corresponding analyses, with all of the steps indicated above performed identically, with only one exception: instead of using Eq. (17), the "pristine signal" is not removed from the total noisy signal. So while Fig. 6 represents *net* transmissibilities, the transmissibilities in Fig. 7 are considered *absolute*. It is immediately apparent that the $1X$ component (that is largely absent in the *net* transmissibilities in Fig. 6) dominates, as expected, because the $1X$ component signifies the persistent steady-state oscillatory response, as shown in the insets of Fig. 4. The $1X$ components are sufficiently large to be on par with the other large responses (of course, that depends on the parameters in Table 1). Figures 6 and 7 substantiate the need for "pristine" models (i.e., analyses such as in Ref. [41]) to evaluate the steady-state performances with and without noise excitation.

It is concluded that the investigated seal, with the parameters listed in Table 1, is less sensitive to noisy excitation at shaft speeds lower than 2000 rad/s, as no appreciable adverse influences are detected in the waterfall plots. At speeds higher than 2000 rad/s, design changes might be necessary to offset detrimental sensitivities to machine vibration. That is manifested by the increased leakages and recurrent faces contacts, both of which signpost seal failure. Such a sensitivity analysis has to be conducted on a case-by-case basis for each seal having similar or additional operational objectives. The outcomes and conclusions are likely to be greatly influenced by the respective parameters. Also, it is important to mention that the current tools as developed herein are completely applicable to gas-lubricated seal. However, the only analytical component that needs to be replaced is the use of the appropriate Reynolds equation (for compressible fluids), and that is a significantly more complicated solution process that requires intricate analytical and numerical procedures [29–31,33,34,53].

4 Conclusion

The objective herein is to provide the theory behind the numerical tools and procedures to investigate the effects that machine vibration imposes upon mechanical face seal transients. Seals sensitivities to noisy machinery are commonly witnessed (diagnosed) in field operation, where noise is a persistent cause for seal deterioration and failure. This is the first time that modeling tools enable to quantify such sensitivities. The analysis builds upon and augments existing comprehensive models that have been developed for "pristine" operation. The noise is generated by a novel use of the Weierstrass–Mandelbrot fractal function. That allows for the exact implementation (calculations) of the noise time derivatives, as they are explicitly needed in the analysis. A unique method is also introduced to calculate the faces contact pressure as a continuous function of the film thickness accounting for surfaces roughness. For this highly nonlinear system, the analysis focuses upon the resultant response about an equilibrium state. It is clearly evident that at about the half-frequency whirl, *X*/2, and the synchronous speed, 1*X*, there are expected strong sensitivities to machine noise. Machine noises, however, result in rich dynamic sensitivities at other sub-synchronous and super-synchronous speeds. The *nX* harmonic components have increased sensitivities with the increase of shaft speeds. These harmonics are attributed to the hydrodynamic effects, steady-state responses to forcing misalignments, and rubbing contact of the seal faces. While the former cause excessive leakage, the latter are utterly detrimental to seal survivability. The results herein are specific to the sample seal analyzed. Other seal designs are likely to possess dynamic attributes that are similar, along with additional attributes that are specific to a dedicated design or an application. The tools developed herein will have to be employed for every seal design on a case-by-case basis. While the sample seal used in the current work is specific for an incompressible fluid (water at 20 °C), the tools developed herein are equally applicable for gas-lubricated mechanical seals, only that the compressible form of the Reynolds equation needs to be used instead. The implementation of the Weierstrass–Mandelbrot fractal function for noise generation can be implemented to model any noisy dynamical system.

Conflict of Interest

There are no conflicts of interest.

Data Availability Statement

The datasets generated and supporting the findings of this article are obtainable from the corresponding author upon reasonable request.

Nomenclature

f = coefficient of friction, Eq. (5)
g = fractal density parameter
h = local film thickness, Table 1
m = stator mass, Table 1
n = index of summation
p = pressure
r = radial coordinate, Table 1 and Figs. 1 and 2
t = time
B = balance ratio, Table 1
C = centerline varying clearance, $C_o + Z$
D = fractal dimension
F = force, Table 1
H = power (heat generation)
I = transverse moment of inertia
M = moment
Q = flow
Z = stator absolute axial degree-of-freedom, Figs. 1 and 2
z_a = root mean square of noise
A_a = fractal noise scale
C_o = design clearance, Table 1
D_{Zs} = support axial damping coefficient, Table 1
K_{Zs} = support axial stiffness coefficient, Table 1
Z_h = axial housing vibration, Figs. 1 and 2
Z_r = axial rotor (shaft) vibration, Figs. 1 and 2
β = face coning, Table 1
γ = relative misalignment, $\vec{\gamma} = \vec{\gamma}_s - \vec{\gamma}_r$
γ_o = relative misalignment caused by rotor runout alone
γ_r = rotor runout, Table 1 and Fig. 1
γ_s = stator nutation, Fig. 1
γ_{si} = stator initial misalignment
γ_{sI} = steady-state stator response due to γ_{si} alone
γ_{sr} = steady-state stator response due to γ_r alone
Δ = difference between noisy and pristine signals, Eq. (17)
θ = angular coordinate
μ = viscosity, Table 1
τ = thermal time constant, Table 1
ψ = precession
ω = frequency or interference in the Appendix
ω_{ref} = shaft angular velocity at steady-state, Table 1

Subscripts

a = housing or rotor
c = contact
g = gyration radius
i = at inner radius
min = minimum film thickness
o = at outer radius
r = rotor
ref = reference value
s = stator or flexible support

Appendix: The Contact Pressure Between Seal Faces

Jackson and Green [46] extend a finite element study of flattening elasto-plastic hemispherical contact to rough surfaces contact and show that hardness is a function of not only the material properties but also of the deformation [45]. The approach in Ref. [46] adopts the stochastic conversion of two rough surfaces into one composite rough surface that is brought into contact with a rigid flat surface adhering to the principles of the Greenwood and Williamson model [54,55]. Accordingly, the interference between each asperity and the contacting rigid flat is $\omega = z - d$, where d is the general surface separation distance. Hence, if h(r, θ, t) is the local temporal film thickness between the seal faces, then $d = h - y_s$. That is depicted in Fig. 8, where $y_s = 4m_2/(\pi m_4)^{1/2}$, and m_2 and m_4 are the second and fourth spectral moments [43,54] of the composite surface roughness [55].

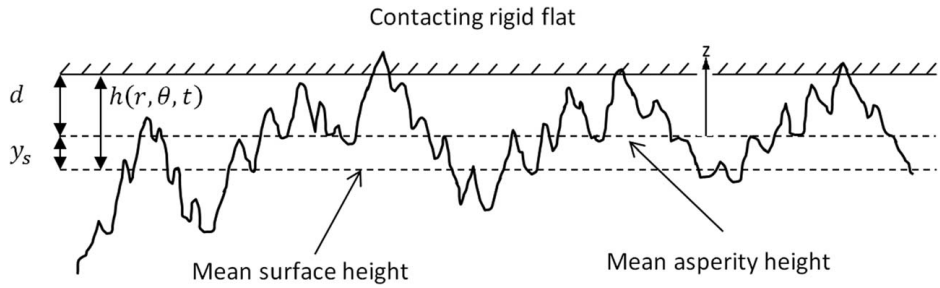

Fig. 8 Contact between a rigid flat and a composite rough surface

The spectral moments m_0, m_2, and m_4, which are calculated in either the spatial or the spectral domains (see Refs. [43,44]), allow the calculation according to Refs. [54,56] of the surface heights RMS, σ, the asperity composite radius of curvature, R, and the areal asperity density, η (as they are given in Table 1). Commensurate with the Greenwood–Williamson model, it is assumed that the asperity heights obey a Gaussian distribution function given by

$$\phi(z/\sigma) = \frac{1}{\sqrt{2\pi}}\left(\frac{\sigma}{\sigma_s}\right)\exp\left[-0.5\left(\frac{\sigma}{\sigma_s}\right)^2\left(\frac{z}{\sigma}\right)^2\right],$$
$$\sigma_s^2 = \sigma^2 - \frac{3.717\times10^{-4}}{\eta^2 R^2} \tag{21}$$

The following critical interference, ω_c, denotes the interference where asperity yielding first occurs, and that is calculated using the von Mises yield criterion [45]:

$$\omega_c = \left(\frac{\pi C S_y}{2E}\right)^2 R \tag{22}$$

Virtually all mechanical face seals have dissimilar materials for the stator and the rotor, possessing distinct Poisson ratios, ν, and yield strengths, S_y. Green [57] teaches that the product CS_y in Eq. (22) is chosen according to $CS_y = \min(C(\nu_1)S_{y1},\ C(\nu_2)S_{y2})$ for surfaces 1 and 2 to account for disparate material properties. The Poisson ratio constant, $C(\nu)$, is calculated for each surface according to Refs. [45,57] as $c(\nu) = 1.295\exp(0.736\nu)$, and $E = [E_1/(1-\nu_1^2) + E_2/(1-\nu_2^2)]^{-1}$ is the equivalent elastic modulus for the composite surface that is in contact with the rigid flat. Using this critical interference, the critical contact force at the onset of yielding is

$$\bar{F}_{cy} = \frac{4}{3}\left(\frac{R}{E}\right)^2\left(\frac{1}{2}\pi C S_y\right)^3 \tag{23}$$

where the over-bar denotes quantities provided for single-asperity contact. The plasticity index, ψ, quantifies the propensity of plasticity to occur during asperity deformation. The index, defined in Ref. [55], is augmented to utilize the yield strength (instead of the hardness):

$$\psi = \frac{2E\sqrt{\sigma_s/R}}{1.639\pi S_y} \tag{24}$$

For the parameters defined in Table 1, the plasticity index is $\psi = 6.2$. Because $\psi > 1$, the faces asperities are likely to deform plastically upon contact. As shown by Jackson and Green [45], the contact force is commensurate to the Hertzian model for deformations in the range of $0 \le \omega \le 1.9\omega_c$, while for $1.9\omega_c < \omega$, an elasto-plastic contact force prevails. Hence,

$$\bar{F}(\omega) = \begin{cases} \bar{F}_{cy}\left(\dfrac{\omega}{\omega_c}\right)^{3/2} & \leftrightarrow \quad 0 \le \left(\dfrac{\omega}{\omega_c}\right) \le 1.9 \\ \bar{F}_{cy}\left\{\left[\exp\left(-\dfrac{1}{4}\left(\dfrac{\omega}{\omega_c}\right)^{5/12}\right)\right]\left(\dfrac{\omega}{\omega_c}\right)^{3/2} + \dfrac{4H_G}{CS_y}\left[1-\exp\left(-\dfrac{1}{25}\left(\dfrac{\omega}{\omega_c}\right)^{5/9}\right)\right]\left(\dfrac{\omega}{\omega_c}\right)\right\} & \leftrightarrow \quad 1.9 < \left(\dfrac{\omega}{\omega_c}\right) \end{cases} \tag{25}$$

where an updated value is taken from Ref. [58] for the ratio between hardness and yield strength:

$$\frac{H_G}{S_y} = 2.84 - 0.92\left[1-\cos\left(\pi\frac{a}{R}\right)\right] \tag{26}$$

along with

$$\frac{a}{R} = \frac{\pi C S_y}{2E}\sqrt{1.9\left(\frac{\omega}{\omega_c}\right)^{1+B}} \quad \text{and} \quad B = 0.14\exp(23S_y/E) \tag{27}$$

Equation (26) indicates that the hardness H_G depends on both, the material and surface properties, along with the deformation magnitude indicated by the radius of contact, a. When the rigid flat and composite rough surfaces are separated by a distance $d = h - y_s$, any asperity whose height exceeds d contacts the rigid flat. Thus, the contribution of all asperities of height z towards the contact force at (r, θ) is

$$\tilde{F}(z, r, \theta) = NA_n\bar{F}(z-d)\phi(z) \tag{28}$$

where A_n is the nominal contact area. Thus, the total contact force at a prescribed surface separation distance is found by summing the contribution of all asperities whose height exceeds the surface separation distance. This summation is achieved by integrating Eq. (28) over the entire vertical contact range (i.e., all asperity heights above d):

$$F(r, \theta) = \eta A_n\int_d^\infty \bar{F}(z-d)\phi(z)dz \tag{29}$$

Rather than evaluate the nominal contact area A_n at every time-step during the simulations, Eq. (29) is redefined to calculate the

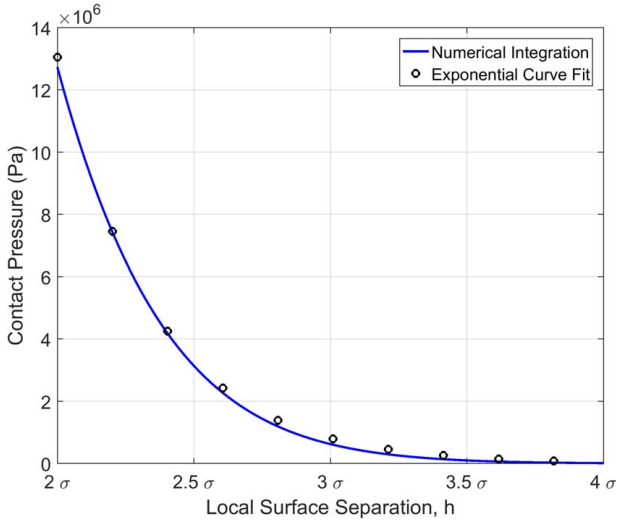

Fig. 9 Comparing the numeric and approximated contact pressure for the seal data in Table 1 ($\sigma = 0.1\ \mu$m)

average contact pressure, $p_c(r, \theta) = F(r, \theta)/A_n$:

$$p_c(r, \theta) = \eta \int_d^\infty \bar{F}(z - d)\phi(z)dz \tag{30}$$

Note that the resulting contact pressure is quasi-static because asperity inertial effects and hysteresis from loading-unloading are neglected. Thus, the contact force only depends on the instantaneous clearance between the approaching surfaces. In general, the film thickness, $h(r, \theta, t)$, between the approaching surfaces is a function of both surface location and time because $h(r, \theta, t)$ depends on the degrees-of-freedom. However, the composite surface roughness is independent of those, as it is assumed of being homogenous, isotropic, and stationary. Hence, a quasi-static contact law permits the contact pressure to be curve-fit versus the local surface film thickness, $h(r, \theta, t)$. This approach radically reduces computation time when solving the system equations of motion because the numerical integration of Eq. (30) is performed once rather than at every nodal point (r, θ) at every time-step in the simulation. Here, an exponential curve-fit is performed on the contact pressure p_c versus the film thickness, h [49]:

$$p_c(r, \theta) = C_1 \exp\left[-C_2 h(r, \theta)\right] \tag{31}$$

That fit is presumed valid for any time, t. This expression depends only on the surface and material properties. Specifically, for the parameters stated in Table 1, a curve-fit yields the constants $C_1 = 3.5 \times 10^9$ Pa and $C_2 = 2.8 \times 10^7$ m^{-1}. The contact pressure versus clearance relationship of Eq. (31) is shown in Fig. 9 along with the numerically integrated results from Eq. (30). Figure 9 clearly indicates agreement between the numerical integration and the exponential curve-fit. Several general observations are made from that figure. First, the contact pressure increases exponentially as the surfaces draw closer, because more asperities interact. For the Gaussian asperity height distribution considered here, the contact pressure decreases by almost an entire order of magnitude for each additional σ of surface separation distance. Clearly at any $h > 4\sigma$, the contact pressure is virtually nil indicating noncontacting operation. At about $h \approx 3\sigma$ contact initiates, while at any $h < 2\sigma$ it would be considered heavy (even severe) contact that would destroy the seal rather quickly. Because mechanical seals are force-balanced, if and when contact ever occurs, that would normally be at about $h \approx 3\sigma$. Further investigation in Ref. [59] shows that the contact pressure decreases significantly as the plasticity index increases, consequently necessitating a robust elasto-plastic such as given in the foregoing. In summary, the explicit contact pressure expression given in Eq. (31) is replicated in Eq. (3) to be used in the numerical time integration method as conducted in this study. Equation (31) offers a contact pressure that varies continuously as a function of the film thickness and is not handled by an on-off Heaviside function [49,60,61] (which is an inaccurate simplification commonly employed in the field of rotor–stator rub).

References

[1] Durham, O. M., Williams, H. J., and Goldman, J. D., 1990, "Effect of Vibration Failure on Electric-Submersible Pumps Failures," J. Pet. Technol., **42**(2), 186–190.

[2] Kim, B., Kim, J., Kang, D., Baek, H.-K., and Chung, J., 2021, "Reduction of the Squeal Noise From an Automotive Water Pump," Nonlinear Dyn., **104**(4), pp. 3293–3308.

[3] Stefanko, D. B., and Leishear, R. A., 2005, "Relationship Between Vibrations and Mechanical Seal Failures in Centrifugal Pumps," Proceedings of IMECE2005 2005 ASME International Mechanical Engineering Congress and Exposition, Orlando, FL, Nov. 5–11.

[4] Green, I., and Etsion, I., 1983, "Fluid Film Dynamic Coefficients in Mechanical Face Seals," ASME J. Lubr. Technol., **105**(2), pp. 297–302.

[5] Green, I., and Etsion, I., 1985, "Stability Threshold and Steady-State Response of Noncontacting Coned-Face Seals," ASLE Trans., **28**(4), pp. 449–460.

[6] Green, I., and Etsion, I., 1986, "A Kinematic Model for Mechanical Seals With Antirotation Locks or Positive Drive Devices," ASME J. Tribol., **108**(1), pp. 42–45.

[7] Green, I., and Etsion, I., 1986, "Nonlinear Dynamic Analysis of Noncontacting Coned-Face Mechanical Seals," ASLE Trans., **29**(3), pp. 383–393.

[8] Green, I., 1987, "The Rotor Dynamic Coefficients of Coned-Face Mechanical Seals With Inward or Outward Flow," ASME J. Tribol., **109**(1), pp. 129–135.

[9] Green, I., 1990, "Separation Speed of Undamped Metal Bellows Contacting Mechanical Face Seals," Tribol. Trans., **33**(2), pp. 171–178.

[10] Green, I., and Bair, S., 1991, "Dynamic Response to Axial Oscillation and Rotating Seat Runout in Contacting Mechanical Face Seals," Tribol. Trans., **34**(2), pp. 169–176.

[11] Wileman, J., and Green, I., 1991, "The Rotordynamic Coefficients of Mechanical Seals Having Two Flexibly Mounted Rotors," ASME J. Tribol., **113**(4), pp. 795–804.

[12] Green, I., and English, C., 1992, "Analysis of Elastomeric O-Ring Seals in Compression Using the Finite Element Method," Tribol. Trans., **35**(1), pp. 83–88.

[13] Green, I., and English, C., 1994, "Stresses and Deformation of Compressed Elastomeric O-Ring Seals," 14th International Conference on Fluid Sealing, London, UK, Apr. 6–8.

[14] Lee, A. S., and Green, I., 1992, "The Coupling of Shaft and Mechanical Face Seal Dynamics Using the Complex Extended Transfer Matrix Method," Proceedings of the Fourth International Symposium on Transport Phenomena and Dynamics of Rotating Machinery (ISROMAC-4), Honolulu, HI, Apr. 5–8.

[15] Lee, A. S., and Green, I., 1994, "Higher Harmonic Oscillations in a Noncontacting FMR Mechanical Face Seal Test Rig," ASME J. Vib. Acoust., **116**(2), pp. 161–167.

[16] Lee, A. S., and Green, I., 1994, "Rotordynamics of a Mechanical Face Seal Riding on a Flexible Shaft," ASME J. Tribol, **116**(2), pp. 345–351.

[17] Lee, A. S., and Green, I., 1995, "Physical Modeling and Data Analysis of the Dynamic Response of a Flexibly Mounted Rotor Mechanical Seal," ASME J. Tribol., **177**(1), pp. 130–135.

[18] Lee, A. S., and Green, I., 1995, "An Experimental Investigation of the Steady-State Response of a Noncontacting Flexibly Mounted Rotor Mechanical Face Seal," ASME J. Tribol., **117**(1), pp. 153–159.

[19] Wileman, J., and Green, I., 1996, "The Rotor Dynamic Coefficients of Eccentric Mechanical Face Seals," ASME J. Tribol., **118**(1), pp. 215–224.

[20] Wileman, J., and Green, I., 1997, "Steady-State Analysis of Mechanical Seals With Two Flexibly Mounted Rotors," ASME J. Tribol., **119**(1), pp. 200–204.

[21] Green, I., 2001, "Real-Time Monitoring and Control of Mechanical Face-Seal Dynamic Behaviour," Sealing Technol., **2001**(96), pp. 6–11.

[22] Zou, M., and Green, I., 1998, "Real-Time Condition Monitoring of Mechanical Face Seal," Tribol. Series, **34**, pp. 423–430.

[23] Wileman, J., and Green, I., 1998, "Stability Analysis of Mechanical Seals With Two Flexibly Mounted Rotors," ASME J. Tribol., **120**(2), pp. 145–151.

[24] Wileman, J., and Green, I., 1999, "Parametric Investigation of the Steady-State Response of a Mechanical Seal With Two Flexibly Mounted Rotors," ASME J. Tribol., **121**(1), pp. 69–76.

[25] Zou, M., and Green, I., 1999, "Clearance Control of a Mechanical Face Seal," Tribol. Trans., **42**(3), pp. 535–540.

[26] Zou, M., Dayan, J., and Green, I., 1999, "Parametric Analysis for Contact Control of a Noncontacting Mechanical Face Seal," Noise & Structural Dynamics, Venice, Italy, Apr. 28–30.

[27] Dayan, J., Zou, M., and Green, I., 2000, "Sensitivity Analysis for the Design and Operation of a Non-Contacting Mechanical Face Seal," Proc. Inst. Mech. Eng. Part C: J. Mech. Eng. Sci., **214**(9), pp. 1207–1218.

[28] Zou, M., Dayan, J., and Green, I., 2000, "Feasibility of Contact Elimination of a Mechanical Face Seal Through Clearance Adjustment," ASME J. Eng. Gas Turbines Power, **122**(3), pp. 478–484.

[29] Green, I., and Barnsby, R. M., 2001, "A Simultaneous Numerical Solution for the Lubrication and Dynamic Stability of Noncontacting Gas Face Seals," ASME J. Tribol., **123**(2), pp. 388–394.
[30] Miller, B. A., and Green, I., 2001, "Numerical Formulation for the Dynamic Analysis of Spiral-Grooved Gas Face Seals," ASME J. Tribol., **123**(2), pp. 395–403.
[31] Green, I., and Barnsby, R. M., 2002, "A Parametric Analysis of the Transient Forced Response of Noncontacting Coned-Face Gas Seals," ASME J. Tribol., **124**(1), pp. 151–157.
[32] Dayan, J., Zou, M., and Green, I., 2002, "Contact Elimination in Mechanical Face Seals Using Active Control," IEEE Trans. Control Syst. Technol., **10**(3), pp. 344–354.
[33] Miller, B. A., and Green, I., 2002, "Numerical Techniques for Computing Rotordynamic Properties of Mechanical Gas Face Seals," ASME J. Tribol., **124**(4), pp. 755–761.
[34] Miller, B. A., and Green, I., 2003, "Semi-Analytical Dynamic Analysis of Spiral-Grooved Mechanical Gas Face Seals," ASME J. Tribol., **125**(2), pp. 403–413.
[35] Green, I., 2008, "On the Kinematics and Kinetics of Mechanical Seals, Rotors, and Wobbling Bodies," Mech. Mach. Theory, **43**(7), pp. 909–917.
[36] Varney, P., and Green, I., 2017, "Impact Phenomena in a Noncontacting Mechanical Face Seal," ASME J. Tribol., **139**(2), p. 022201.
[37] Varney, P., and Green, I., 2018, "Dynamic Modeling of an Eccentric Face Seal Including Coupled Rotordynamics, Face Contact, and Inertial Maneuver Loads," Proc. Inst. Mech. Eng. Part J: J. Eng. Tribol., **232**(6), pp. 732–748.
[38] Green, I., 1989, "Gyroscopic and Support Effects on the Steady-State Response of a Noncontacting Flexibly Mounted Rotor Mechanical Face Seal," ASME J. Tribol., **111**(2), pp. 200–206.
[39] Jackson, R. L., and Green, I., 2008, "The Thermoelastic Behavior of Thrust Washer Bearings Considering Mixed Lubrication, Asperity Contact, and Thermoviscous Effects," Tribol. Trans., **51**(1), pp. 19–32.
[40] Jackson, R. L., and Green, I., 2006, "The Behavior of Thrust Washer Bearings Considering Mixed Lubrication and Asperity Contact," Tribol. Trans., **49**(2), pp. 233–247.
[41] Green, I., 2002, "A Transient Dynamic Analysis of Mechanical Seals Including Asperity Contact and Face Deformation," Tribol. Trans., **45**(3), pp. 284–293.
[42] Green, I., and Etsion, I., 1986, "Pressure and Squeeze Effects on the Dynamic Characteristics of Elastomer O-Rings Under Small Reciprocating Motion," ASME J. Tribol., **108**(3), pp. 439–444.
[43] Green, I., 2020, "Metrology and Numerical Characterization of Random Rough Surfaces—Data Reduction Via an Effective Filtering Solution," Proc. Inst. Mech. Eng. Part J: J. Eng. Tribol., **234**(9), pp. 1452–1469.
[44] Green, I., 2019, "Exact Spectral Moments and Differentiability of the Weierstrass–Mandelbrot Fractal Function," ASME J. Tribol., **142**(4), p. 041501.
[45] Jackson, R. L., and Green, I., 2005, "A Finite Element Study of Elasto-Plastic Hemispherical Contact Against a Rigid Flat," ASME J. Tribol., **127**(2), pp. 343–354.
[46] Jackson, R. L., and Green, I., 2006, "A Statistical Model of Elasto-Plastic Asperity Contact Between Rough Surfaces," Tribol. Int., **39**(9), pp. 906–914.
[47] Chang, W. R., Etsion, I., and Bogy, D. B., 1987, "An Elastic-Plastic Model for the Contact of Rough Surfaces," ASME J. Tribol., **109**(2), pp. 257–263.
[48] Green, I., 2018, "Discussion: 'Extended Greenwood-Williamson Models for Rough Spheres'(Zhao, T., and Feng, Y. T., 2018, ASME J. Appl. Mech., 85(10), p. 101007)," ASME J. Appl. Mech., **85**(11), p. 115501.
[49] Varney, P., and Green, I., 2016, "Rough Surface Contact of Curved Conformal Surfaces: An Application to Rotor–Stator Rub," ASME J. Tribol., **138**(4), p. 041401.
[50] Berry, M. V., and Lewis, Z. V., 1980, "On the Weierstrass–Mandelbrot Fractal Function," Proc. R. Soc. A, **370**(1743), pp. 459–484 .
[51] Shampine, L. F., 1994, *Numerical Solution of Ordinary Differential Equations*, Chapman and Hall/CRC, New York.
[52] Savitzky, A., and Golay, M. J. E., 1964, "Smoothing and Differentiation of Data by Simplified Least Squares Procedures," Anal. Chem., **36**(8), pp. 1627–1639.
[53] Miller, B., and Green, I., 1998, "Constitutive Equations and the Correspondence Principle for the Dynamics of Gas Lubricated Triboelements," ASME J. Tribol., **120**(2), pp. 345–352.
[54] McCool, J. I., 1987, "Relating Profile Instrument Measurements to the Functional Performance of Rough Surfaces," ASME J. Tribol., **109**(2), pp. 264–270.
[55] Greenwood, J. A., and Williamson, J. B. P., 1966, "Contact of Nominally Flat Surfaces," Proc. R. Soc. Lond. A, **295**(1442), pp. 300–319.
[56] Jackson, R. L., and Green, I., 2011, "On the Modeling of Elastic Contact Between Rough Surfaces," Tribol. Trans., **54**(2), pp. 300–314.
[57] Green, I., 2005, "Poisson Ratio Effects and Critical Values in Spherical and Cylindrical Hertzian Contacts," Appl. Mech. Eng., **10**(3), p. 451.
[58] Jackson, R. L., Green, I., and Marghitu, D. B., 2010, "Predicting the Coefficient of Restitution of Impacting Elastic-Perfectly Plastic Spheres," Nonlinear Dyn., **60**(3), pp. 217–229.
[59] "Analysis of Simultaneous Rotordynamic Faults Using Coupled Mechanical Face Seal Vibration," https://smartech.gatech.edu/handle/1853/56320, Accessed April 8, 2022.
[60] Varney, P., and Green, I., 2015, "Nonlinear Phenomena, Bifurcations, and Routes to Chaos in an Asymmetrically Supported Rotor–Stator Contact System," J. Sound Vib., **336**, pp. 207–226.
[61] Varney, P., and Green, I., 2016, "Rotordynamic Analysis of Rotor–Stator Rub Using Rough Surface Contact," ASME J. Vib. Acoust., **138**(2), p. 021015.